OPEN ACCESS



Evolution of the Inner Accretion Flow and the White Dwarf Spin Pulse during the 2023 Outburst in GK Persei

Mariko Kimura^{1,2}, Takayuki Hayashi^{3,4,5}, Yuuki Wada⁶, Wataru Iwakiri⁷, Shigeyuki Sako^{8,9}, Martina Veresvarska¹⁰, Simone Scaringi¹⁰, Noel Castro-Segura^{11,12}, Christian Knigge¹², Keith C. Gendreau¹³, and Zaven Arzoumanian¹³, Advanced Research Center for Space Science and Technology, College of Science and Engineering, Kanazawa University, Kakuma, Kanazawa, Ishikawa 920-1192, Japan

Cluster for Pioneering Research, Institute of Physical and Chemical Research (RIKEN), 2-1 Hirosawa, Wako, Saitama 351-0198, Japan
 Center for Research and Exploration in Space Science and Technology (CRESST II), Greenbelt, MD 20771, USA
 Department of Physics, University of Maryland, Baltimore County, 1000 Hilltop Circle, Baltimore, MD 21250, USA
 X-ray Astrophysics Division,NASA Goddard Space Flight Center, Greenbelt, MD 20771, USA

Graduate School of Engineering, Osaka University, 2-1 Yamadaoka, Suita, Osaka, 565-0871, Japan
Tinternational Center for Hadron Astrophysics, Chiba University, Chiba 263-8522, Japan

Institute of Astronomy, Graduate School of Science, The University of Tokyo, 2-21-1 Osawa, Mitaka, Tokyo 181-0015, Japan
 The Collaborative Research Organization for Space Science and Technology, The University of Tokyo, 7-3-1 Hongo, Bunkyo-ku, Tokyo 113-0033, Japan
 Centre for Extragalactic Astronomy, Department of Physics, Durham University, South Road, Durham, DH1 3LE, UK

Department of Physics, University of Warwick, Gibbet Hill Road, Coventry, CV 4 7AL, UK
 Department of Physics and Astronomy. University of Southampton, Southampton, SO17 1BJ, UK
 Astrophysics Science Division, NASA Goddard Space Flight Center, Greenbelt, MD 20771, USA
 Received 2024 June 3; revised 2025 April 18; accepted 2025 April 20; published 2025 May 29

Abstract

We present our X-ray and optical observations performed by NICER, NuSTAR, and Tomo-e Gozen during the 2023 outburst in the intermediate polar GK Persei. The X-ray spectrum consisted of three components: blackbody (BB) emission of several tens of eVs from the irradiated white dwarf (WD) surface, a source possibly including several emission lines around 1 keV, and multitemperature bremsstrahlung emission from the accretion column. The 351.3 s WD spin pulse was detected in X-rays, and the observable X-ray flux from the column drastically decreased at the off-pulse phase, which suggests that the absorption of the column by the accreting gas, called the curtain, was the major cause of the pulse. As the system became brighter in the optical, the column became fainter, the pulse amplitude became higher, and the energy dependence of pulses became weaker at <8 keV. These phenomena could be explained by the column's more pronounced absorption by the denser curtain as mass-accretion rates increased. The BB and line fluxes rapidly decreased at the optical decline, which suggests the expansion of the innermost disk edge with decreasing accretion rates. The electron scattering or the column geometry may be associated with the almost no energy dependence of high-energy pulses. The irradiated vertically thick structure at the disk may generate optical quasi-periodic oscillations with a period of ~5700 s.

Unified Astronomy Thesaurus concepts: Cataclysmic variable stars (203); Dwarf novae (418); DQ Herculis stars (407); X-ray sources (1822); Stellar accretion disks (1579)

1. Introduction

Cataclysmic variables (CVs) are close binary systems consisting of a primary white dwarf (WD) and a secondary low-mass star. The secondary star fills its Roche lobe, and the gas transferred from the star usually forms an accretion disk around the WD (see B. Warner 1995, for a comprehensive review). CVs are classified into two types, magnetic CVs and nonmagnetic CVs, by the strength of the WD magnetic field. Intermediate polars (IPs) are one subclass of magnetic CVs hosting a WD with a magnetic field strength of $B \sim 10^{5-7}$ G. In these systems, the inner part of the disk is truncated by the WD magnetic field, and the accreting gas channeled to it directly falls onto the WD along field lines at freefall velocity. A strong shock is formed, and the gas is heated up to a temperature of the order of $\sim 10 \, \text{keV}$. This high-temperature gas is the source of intense X-ray emission from IPs, and is called the accretion column (AC). Some high-energy X-ray

Original content from this work may be used under the terms of the Creative Commons Attribution 4.0 licence. Any further distribution of this work must maintain attribution to the author(s) and the title of the work, journal citation and DOI.

photons from the AC are reflected on the WD surface (K. Mukai et al. 2015; T. Hayashi et al. 2018). Some others are absorbed into the WD surface, and a part of it is heated up, which emits soft X-ray photons of about several tens of eVs (P. A. Evans & C. Hellier 2007; R. Landi et al. 2009).

The X-ray spin pulse observed in IPs is considered to be produced by a change in the absorption to the observer of the AC by the accreting gas from the disk called the curtain. Let us consider that we observe an IP system with a magnetic axis inclined to the WD spin axis. If the AC above the disk equatorial plane points away from the observer, the absorption by the curtain is weak and the observed X-ray flux is the highest (the light maximum at the on-pulse phase). If the AC is in front of the WD to the observer, the absorption by the curtain is strong and the observed X-ray flux is the lowest (the light minimum at the off-pulse phase). Hereafter, we use the terms "on-pulse phase" and "off-pulse phase" as the WD spin phase at the light maximum and that at the light minimum to the observer, respectively. This concept is named the accretion-curtain model (S. R. Rosen et al. 1988; C. Hellier et al. 1991).

Dwarf novae (DNe), a subgroup of CVs, show sudden brightening of the accretion disk, which is called an outburst. It is known that several IPs have entered DN outbursts (see, e.g.,

C. Hellier et al. 1997; R. Ishioka et al. 2002; Y. Tampo et al. 2022). DN outbursts are believed to be caused by the thermalviscous instability in the disk, which is triggered by partial ionization of hydrogen (see J. K. Cannizzo 1993a; Y. Osaki 1996; J.-M. Hameury 2002, for reviews). The thermal equilibrium curve at a given radius of the disk has an unstable branch sandwiched by two stable states: the hot and cool states, corresponding to an outburst state with high accretion rates and a quiescent state with low accretion rates, respectively (F. Meyer & E. Meyer-Hofmeister 1981). The disk is caused to jump between these two states, and transition waves then propagate over the disk (J. Smak 1984; S. Mineshige & Y. Osaki 1985). Although the inner disk is truncated by the WD magnetic field in IPs, this disk-instability model is applicable for their outbursts (J. M. Hameury & J. P. Lasota 2017).

GK Persei (GK Per) is one such IP with DN properties (A. R. King et al. 1979). This system was discovered by its nova eruption in 1901, and is also known as Nova Persei 1901 (G. E. Hale 1901; E. C. Pickering 1901). It was identified as an IP by detection of the 351 s X-ray spin pulse originating from the WD rotation (M. G. Watson et al. 1985). After this eruption, GK Per remained in an almost constant-luminosity state of around 13 mag for \sim 50 yr and started showing DN outbursts after that. The outbursts in GK Per have a smaller amplitude and longer duration than a typical one, and are characterized by a slow rise. GK Per is also known to show quasi-periodic oscillations (QPOs; M. G. Watson et al. 1985; L. Morales-Rueda et al. 1999; D. Nogami et al. 2002; P. Zemko et al. 2017). A recent dynamical mass study by A. Álvarez-Hernández et al. (2021) showed that the orbital period (P_{orb}) , the inclination angle (i), the WD mass (M_1) , and the binary mass ratio ($q \equiv M_2/M_1$) of GK Per are 1.997 days, 67(5) deg, $1.03^{+0.16}_{-0.11} M_{\odot}$, and 0.38(3), respectively. Here, M_2 is the mass of the secondary star. The distance to the source was measured to be 434 ± 8 pc by Gaia Data Release 3 data (Gaia Collaboration et al. 2023). The orbital period is exceptionally long for a CV, as they are mostly less than 12 hr in the standard evolutionary scenario (H. Ritter & U. Kolb 2003; C. Knigge et al. 2011).

Recently, GK Per commenced outbursting every few years, exhibiting a new outburst in 2023 January. This outburst was bright at X-ray and optical wavelengths, and provided the best opportunity for detailed timing analyses. We performed observations during this outburst using the X-ray telescope NICER (K. C. Gendreau et al. 2016), the X-ray satellite NuSTAR (F. A. Harrison et al. 2013), and an optical wide-field CMOS camera called Tomo-e Gozen (S. Sako et al. 2018). We aim to address the following unsolved problems pointed out in previous works: whether the standard disk-instability model can explain the peculiar outbursts in this system, whether the photoelectric absorption of X-ray photons by the curtain can reproduce the entire nature of the spin pulse, and from where its complex X-ray emission and QPOs originate (L. Morales-Rueda et al. 1999; D. Nogami et al. 2002; S. Vrielmann et al. 2005; T. Yuasa et al. 2016; P. Zemko et al. 2017; S. Pei et al. 2024).

This paper is structured as follows. Section 2 describes the observations and data reduction. Section 3 shows our results for the X-ray and optical timing analyses and modeling of X-ray spectra. In Section 4, we discuss the outburst mechanism, the X-ray emission source, and the origins of spin pulses and other periodic signals. We give a summary in Section 5.

Table 1
Log of Observations of GK Per with NICER

Bog of Cost validity of Off for Will Problet					
NICER ObsID	Start ^a	Enda	On-source Time ^b	Average Rate ^c	
5202530101	58.3383	58.4635	2515	11.1	
5202530102	58.5963	58.9138	6286	23.1	
5202530103	60.3264	60.3333	600	13.2	
5202530104	60.6493	61.1716	995	15.5	
5202530105	62.1349	62.4614	680	13.3	
5202530106	62.5225	63.4288	1968	16.1	
5202530107	63.7492	64.0740	308	17.7	
5202530108	64.9670	65.4932	1413	17.8	
5202530109	68.3303	68.3317	121	12.3	
5202530110	68.9740	68.9768	240	19.4	
5202530111	69.7450	70.4604	1119	13.9	
5202530112	70.7767	71.0409	811	15.8	
5202530113	71.7446	72.3288	1304	18.5	
5202530114	72.5831	73.4919	2056	16.2	
5202530115	73.6161	74.2637	868	16.0	
5202530116	74.5196	74.9732	639	13.5	
5202530117	75.6795	76.1342	860	15.4	
5202530118	77.8059	77.8780	1329	15.5	
5202530119	80.3191	80.3339	1177	16.1	
5202530120	80.9633	80.9711	675	12.9	
5202530121	81.9367	82.1347	2002	16.8	
5202530122	83.2265	83.2322	500	9.2	
5202530123	83.5495	84.2037	4435	14.0	
5202530124	84.6403	84.7231	4014	11.9	
5202530125	85.6725	85.6991	2305	17.4	
5202530126	86.6447	87.1731	2631	15.4	
5202530127	87.6719	88.2050	2951	19.0	
5202530128	88.9092	89.4339	1853	17.3	
5202530129	89.6920	89.8111	1336	13.8	
5202530130	91.5416	91.6942	3776	17.1	
5202530131	93.7371	94.0717	3878	11.8	
5202530132	94.9593	95.0356	2456	12.7	
5202530133	96.9594	97.0412	3007	13.1	
5202530134	97.9999	98.0728	1402	12.2	
5202530135	98.9675	99.0329	281	10.2	

Notes.

2. Observations and Data Reduction

2.1. NICER

Hereafter, all observation times are converted to barycentric Julian date (BJD). The X-ray telescope NICER on board the International Space Station (ISS) monitored GK Per during its 2023 outburst, starting from BJD 2459958. The NICER effective area around 1 keV is larger than the Swift one by \sim 10 times. The observation IDs of the monitoring are given in Table 1. This work used HEAsoft version 6.31.1 including FTOOLS (J. K. Blackburn et al. 1999) for data reduction and analyses.¹⁴ The data were reprocessed with the pipeline tool nicer12, which used a NICER Calibration Database (CALDB) version later than 2022 October 31 for producing light curves and time-averaged spectra. NICER is composed of 56 modules of silicon drift detectors, 52 of which are operating in orbit, including two noisy modules, IDs 14 and 34. In our data reduction process with nicer12, we filtered out the data of these two modules. The light curves were generated by

^a BJD 2459900.0.

^b Units of seconds.

^c NICER count rate in 0.3-7 keV band in units of counts s⁻¹.

¹⁴ https://heasarc.gsfc.nasa.gov/ftools/

Table 2
Log of Observations of GK Per with NuSTAR

NICER ObsID	Start ^a	Enda	On-source Time ^b	Average Rate ^c
90901305002	97.6959	98.6047	43191	1.18

Notes.

- ^a BJD 2459900.0.
- ^b Units of seconds.
- ^c NuSTAR count rate in 3–79 keV band in units of counts s⁻¹.

lcurve. The source and background spectra were extracted with nibackgen3C50 version 7. For the spectral analyses, we obtained a response matrix file and an ancillary response file for a specific set of 50 detectors to match the default settings of the background model.¹⁵

2.2. NuSTAR

The NuSTAR Target of Opportunity observations were carried out on 2023 February 22 (ObsID 90901305002). The observation log is given in Table 2. The observation time was partially overlapped with that of the NICER observation of ObsID 5202530134 on the same day. The data were reprocessed with nupipeline and the NuSTAR CALDB as of 2022 May 10. The light curves, time-averaged spectra, and response and ancillary response files were obtained with nuproducts. The background region was circular with a radius of 100" on a blank sky area. We determined the circular source region centered at the target position with a 50" radius.

2.3. Tomo-e Gozen

Tomo-e Gozen is an optical wide-field video observation system composed of 84 CMOS image sensor chips on the 1.05 m Kiso Schmidt telescope (S. Sako et al. 2018). This system is capable of obtaining consecutive frames with timestamps of 0.2 ms absolute accuracy. The frame rate is increased by reading a part of the pixels of the image sensor. We observed GK Per at 19 frames per second. The observation log is given in Table 3.

After dark subtraction and flat-fielding for the raw data, we extracted the light curve by using the Photutils python package (L. Bradley et al. 2024). We stacked every 10 frames to a 0.5 s exposure, searched for bright stars in each stacked frame, and queried their G-band magnitudes from Gaia Early Data Release 3 catalog (Gaia Collaboration et al. 2021). The background was subtracted by SExtractor. 16 We made a diagram of the G magnitude versus the measured count for several bright stars, and estimated the zero count C_{zero} corresponding to 0 mag. We performed relative photometry for the target by using the C_{zero} curve. Since Tomo-e Gozen is sensitive to rapid time variations of the sky condition, we need to perform relative photometry for the target with several reference stars in the same image to check whether the sky condition affects the target light curve or not. If the sky condition is bad, C_{zero} fluctuates. We removed these outlier points.

2.4. AAVSO Data

We also used optical data obtained by the American Association of Variable Star Observers (AAVSO). The AAVSO archive data are available online. ¹⁷ Each observer performed the relative photometry by using nearby comparison stars. The magnitude of each comparison star was measured by the AAVSO Photometric All-Sky Survey (A. A. Henden et al. 2016) from the AAVSO Variable Star Database. ¹⁸

3. Results

3.1. Overall Outburst Behavior

The optical light curve and the B-V color evolution during the 2023 outburst are shown in Figure 1 in comparison with those in previous outbursts. The outburst light curve seems to be composed of three parts: an early phase of the rising part (a steeper rise) during days 0–15, a later phase of the rising part (a slower rise) during days 15–48, and a rapid decline during days 48–66. The rising or fading rates of these three parts are -9.6, -26.1, and 9.0 day mag⁻¹, respectively. The B-V color became bluest around the outburst maximum.

We compared the optical and X-ray light curves during the 2023 outburst in Figure 2. The X-ray flux in the 0.3–8 keV band seemed constant during this outburst (see the middle panel of Figure 2), which may be similar to that in the 2018 outburst (S. Pei et al. 2024). The 0.3–1 keV flux basically traced the optical light curve (see white circles in the bottom panel). On the other hand, the 2–8 keV light curve was anticorrelated with the optical light curve (see blue triangles in the same panel). The 1–2 keV flux began to increase in the middle of the fading stage (see black rectangles in the same panel).

3.2. Broadband X-Ray Spectral Analyses

We obtained partially overlapped NICER and NuSTAR observations on BJD 2459998 (see also the purple line in Figure 2). We cut the NICER spectrum including the data taken during ISS daytime below 0.4 keV because of high background rates. Empirically, X-ray spectra from IPs have been modeled by a cooling-flow model, which is a kind of multitemperature thin thermal plasma model (e.g., T. Hayashi et al. 2011; A. Dobrotka et al. 2017; M. Tsujimoto et al. 2018). We fitted the spectra with the model Tbabs* (bbody + gaussian + pwab* (reflect*vmcflow + gaussian)) in the XSPEC software (K. A. Arnaud 1996), where Tbabs, pwab, bbody, reflect, and vmcflow denote X-ray absorption by the interstellar medium, partial X-ray absorption by the intrinsic medium to the object, blackbody (BB) radiation, a convolution model for reflection from neutral material, and a cooling-flow model, respectively. The first and second gaussian models represent the oxygen fluorescence $K\alpha$ line at 0.53 keV and the iron fluorescence $K\alpha$ line at 6.4 keV, respectively. The line center energies of these models are fixed. As for the former emission line, the line-width parameter σ is fixed at 0.001 keV because of the limitation of NICER energy resolution.

We fit eight NICER spectra averaged per 5 days by tying the column-density parameter $N_{\rm H}$ in the Tbabs model, and

¹⁵ The method is described online at https://heasarc.gsfc.nasa.gov/docs/nicer/analysis_threads/arf-rmf/, and we use the additional data version xti20200722.

¹⁶ https://www.astromatic.net/software/sextractor/

¹⁷ http://www.aavso.org/data/download/

¹⁸ http://www.aavso.org/vsp/

Table 3Log of Observations of GK Per with Tomo-e Gozen

Date	Start ^a	End ^a	On-source Time ^b	Average Magnitude ^c
2023-02-17	92.9807	93.0407	2854	12.0
2023-02-21	96.9583	97.0439	3821	12.1
2023-02-22	98.0550	98.0676	1090	12.3
2023-02-23	98.9521	99.0357	3821	12.3

Notes.

^a BJD 2459900.0.

^b Units of seconds.

^c Magnitude without a filter. The sensitive wavelengths are 380-710 nm.

Table 4

Best-fit Parameters for Models of Tbabs* (bbody + gaussian + pwab* (reflect*vmcflow + gaussian)) in the Spectral Model Fitting of the Simultaneous NICER and NuSTAR Observation Data of GK Per on BJD 2459998 (2023 February 22)

*	• '
Parameter	Best-fit Value
$N_{ m H}^{\ \ a}$	0.16 (fixed)
$T_{ m BB}{}^{ m b} \ L_{ m BB}{}^{ m c}$	$83^{+5.7}_{-5.3} \\ 0.56^{+0.15}_{-0.16}$
$N_{ m H,min}^{a}$ $N_{ m H,max}^{a}$	$0.34 \pm 0.01 \\ 10.7^{+0.46}_{-0.75}$
$\Omega/2\pi^{\mathrm{d}}$ $\cos i^{\mathrm{e}}$	1.0 (fixed) 0.39 (fixed)
kT_1^{f} Z_0^{g} $\dot{M}_{ m acc}^{ ext{h}}$	$54.1_{-0.6}^{+2.3} 0.48_{-0.07}^{+0.06} 6.4_{-0.1}^{+0.2} \times 10^{-10}$
$E_1^{\ i} \ \sigma_1^{\ j} \ ext{Norm}_1^{\ k}$	0.53 (fixed) 0.001 (fixed) $(6.1\pm1.1) \times 10^{-4}$
$E_2^{\ \mathrm{i}} \ \sigma_2^{\ \mathrm{j}} \ \mathrm{Norm_2}^k$	6.4 (fixed) 0.18 ± 0.02 $(3.3^{+0.2}_{-0.1}) \times 10^{-4}$
	1.54
	$N_{ m H}^{ m a}$ $T_{ m BB}^{ m b}$ $L_{ m BB}^{ m c}$ $N_{ m H,min}^{ m a}$ $N_{ m H,max}^{ m a}$ $\Omega/2\pi^{ m d}$ $\cos i^{ m c}$ $kT_{ m 1}^{ m f}$ $Z_{ m O}^{ m g}$ $\dot{M}_{ m acc}^{ m h}$ $E_{ m 1}^{ m i}$ $Norm_{ m 1}^{ m k}$ $E_{ m 2}^{ m i}$ $\sigma_{ m 2}^{ m j}$

Notes. The errors represent 90% confidence ranges. Gaussians 1 and 2 denote oxygen and iron fluorescence lines, respectively.

estimated it as $1.6 \times 10^{21} \, \mathrm{cm}^{-2}$ (see also Section 3.3), which is consistent with the value reported by past works (P. Zemko et al. 2017; S. Pei et al. 2024). Hereafter, we fixed N_{H} in that model at this value. Also, we fixed the solid angle of the reflector subtending the hot plasma to 1, which corresponds to the parameter $\Omega/2\pi$ in the reflect model, by assuming the reflector is the WD. Since the accretion rate onto the WD in

GK Per is high during outburst, the AC height is as low as <10% of the WD radius (V. Suleimanov et al. 2016; Y. Wada et al. 2018). We tied the abundance Z in the reflect model and the oxygen abundance $Z_{\rm O}$ in the vmcflow model. The iron and nickel abundances were fixed at 0.105 and 0.1, respectively, which were estimated by P. Zemko et al. (2017). The best-fit model parameters are summarized in Table 4.

We found that the BB emission was dominant at less than 1 keV. The best-fit temperature and radius were 78 eV and 5.3×10^{5} cm, respectively. The irradiated region was only 0.0001% of the WD surface, and the temperature of the irradiated WD surface was much higher than the typical temperature of nonirradiated WDs in CVs during outbursts, which is \sim 40,000 K (see Table 2.8 in B. Warner 1995; P. Godon et al. 2017). Here, we assume that the radius of a $\sim 1 \, M_{\odot}$ WD in GK Per is 5×10^8 cm (M. Nauenberg 1972; A. Álvarez-Hernández et al. 2021). The optically thin and multitemperature bremsstrahlung emission was dominant above 1 keV. The maximum temperature was 54 keV, and the mass-accretion rate was $6.4 \times 10^{-10} M_{\odot} \text{ yr}^{-1}$. These values are close to previously reported parameter values in the quiescent state (P. Zemko et al. 2017; Y. Wada et al. 2018; S. Pei et al. 2024). This would be because this spectrum was taken at the end of the outburst. The unabsorbed flux in the $0.3-50\,\mathrm{keV}$ band was $5.0\times10^{-10}\,\mathrm{erg}\,\mathrm{s}^{-1}\,\mathrm{cm}^{-2}$, which corresponds to an X-ray luminosity of $1.1 \times 10^{34} \,\mathrm{erg \, s^{-1}}$.

3.3. Evolution of X-Ray Spectra

We also tried to model the NICER spectra averaged per 5 days to investigate the time evolution of each spectral component. Eight spectra were obtained, with each spectrum numbered as S1, S2, S3, S4, S5, S6, S7, and S8, respectively, from the earliest to the latest. These time intervals are denoted in the top panel of Figure 3. We needed to add neon, iron, magnesium, and silicon emission lines to the model, which were prominent in the bright state during previous outbursts (S. Vrielmann et al. 2005; P. Zemko et al. 2017). The line width was comparable with the energy resolution (~0.1 keV around 1 keV), and the detailed structure, e.g., the He-like triplet, was not resolved (see Figure 4).

We modeled the averaged NICER spectra using the model Tbabs* (gaussian + gaussian + bbody + gaussian + gaussian)). The power-law model is a simple photon power-law (PL) model. We added this model instead of the vmcflow model since it is hard to determine $T_{\rm max}$ only with the NICER spectrum below

^a Equivalent hydrogen column in 10²² atoms cm⁻².

^b Blackbody temperature in eV.

^c Blackbody luminosity, L_{36}/D_{10}^2 , where L_{36} is the source luminosity in units of 10^{36} erg s⁻¹ and D_{10} is the distance to the source in units of 10 kpc.

d Reflection scaling factor.

^e Here, *i* denotes the inclination angle of the system, and we applied i = 67 deg. ^f Plasma temperature in keV.

^g Oxygen abundance with respect to the solar one.

^h Mass-accretion rate in units of solar masses per year (\dot{M}_{\odot} yr⁻¹).

i Line energy in keV.

j Line width in keV.

k Total photons cm⁻² s⁻¹ in the line.

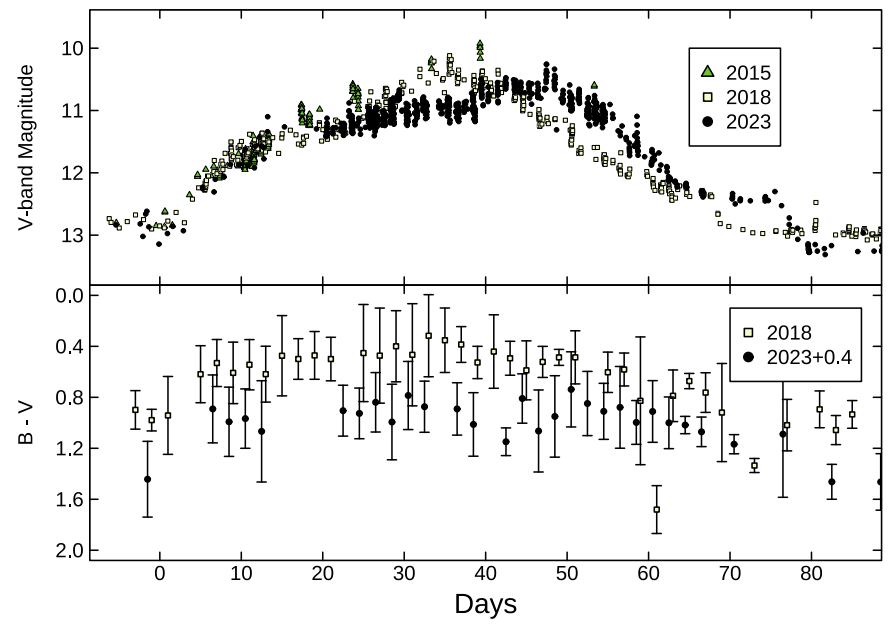


Figure 1. Overall optical V-band light curves and B - V color evolution during outbursts in GK Per. The data were provided by the AAVSO. The upper panel shows light curves during the 2015, 2018, and 2023 outbursts. The lower panel shows the B - V color evolution during the 2018 and 2023 outbursts. The triangle, rectangle, and circle represent the data of the 2015, 2018, 2023 outbursts, respectively.

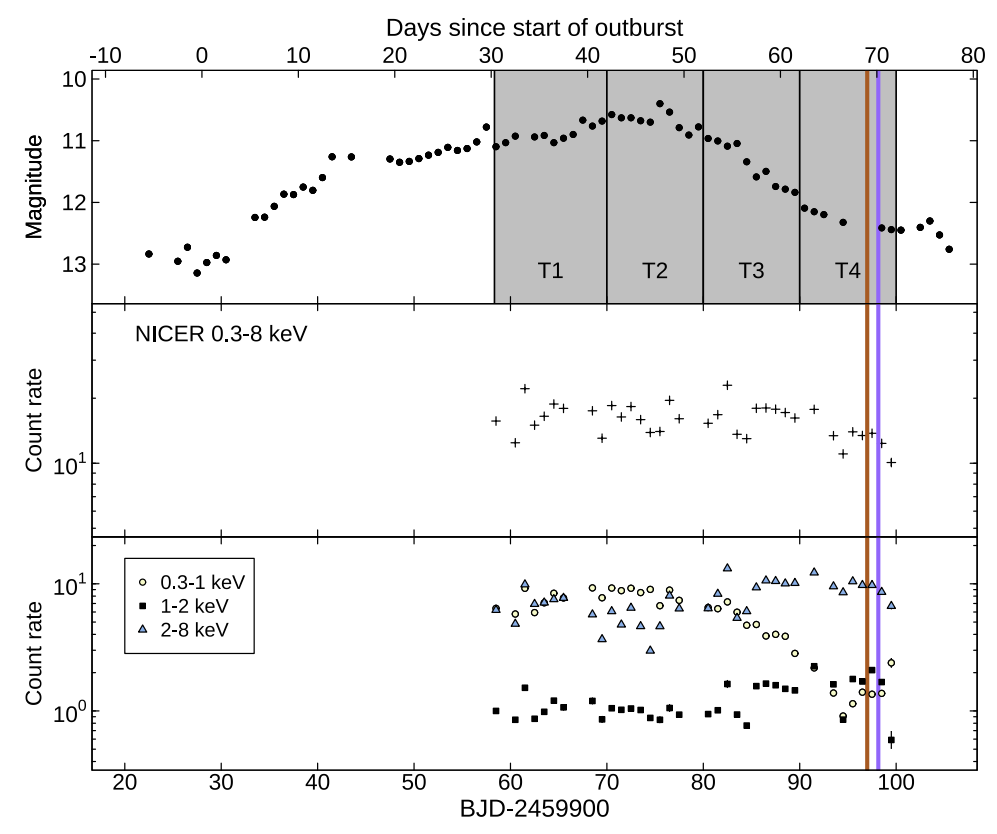


Figure 2. Overall optical *V*-band light curves (top panel), NICER X-ray light curves in the 0.3–8 keV (middle panel), and 0.3–1 keV, 1–2 keV, and 2–8 keV bands (bottom panel) during the 2023 outburst in GK Per. In the bottom panel, the white circle, black rectangle, and blue triangle represent the 0.3–1 keV, 1–2 keV, and 2–8 keV light curves, respectively. The data are averaged per day. The orange and purple lines indicate the time of simultaneous observations by NICER and Tomoe-Gozen, and by NICER and NuSTAR, respectively. Here, T1, T2, T3, and T4 represent the time zones before BJD 2459970, BJD 2459970–2459980, BJD 2459980–2459990, and BJD 2459900–2460000, respectively. We divide the data into these time zones in Section 3.5 in order to explore the time evolution of WD spin pulses.

7 keV. Since we aimed to investigate the change in the absorption effect, we fixed the photon index at 1.48 for all spectra. This value was derived from modeling with the PL

model of the best-fit vmcflow model for the simultaneously observed NICER and NuSTAR spectrum presented in Figure 5 and Table 4. We confirmed that this slope does not change if

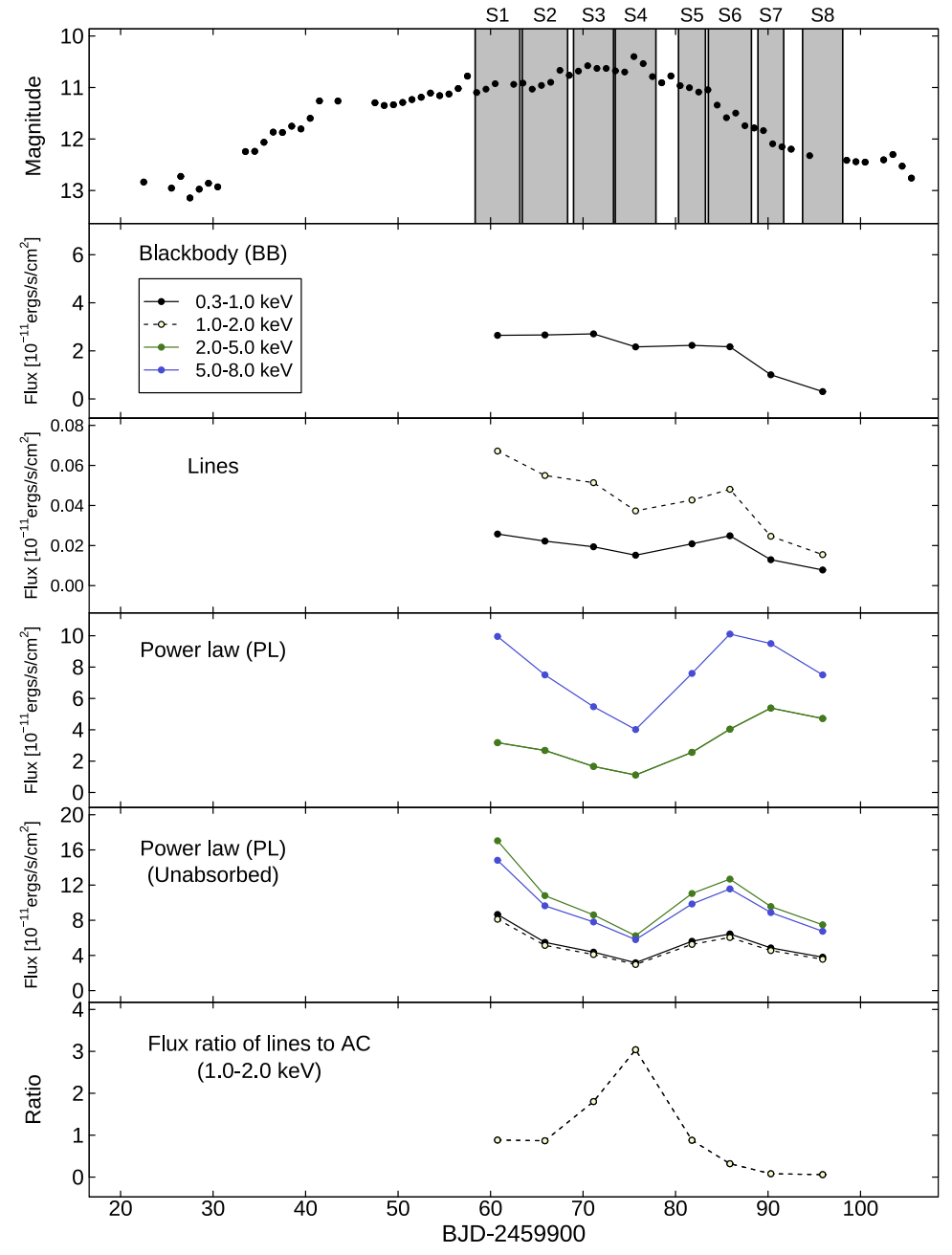


Figure 3. Optical light curves (top panel), X-ray fluxes of the best-fit model components in the 0.3–1 keV, 1–2 keV, 2–5 keV, and 5–8 keV bands (second, third, fourth, and fifth panels), and the flux ratio of neon, magnesium, iron, and silicon emission lines to the sum of the power law and three Gaussian components in the 1–2 keV band (bottom panel). Here, we omit some model flux curves if they have little contribution. S1, S2, S3, S4, S5, S6, S7, and S8 represent the time zones BJD 2459958.3–2459963.2, BJD 2459963.4–2459968.3, BJD 2459969.0–2459973.3, BJD 2459973.5–2459977.9, BJD 2459980.3–2459983.2, BJD 2459988.9–2459991.7, and BJD 2459993.7–2459998.1, respectively. We divide the data into these time zones in order to investigate the time evolution of X-ray spectra.

 $T_{\rm max}$ is higher than 10 keV. This condition was satisfied in previous outbursts of GK Per (T. Yuasa et al. 2016; Y. Wada et al. 2018; S. Pei et al. 2024). The abundance Z in the reflect model was fixed at the best-fit $Z_{\rm O}$ value obtained in Section 3.2.

The line center energies of the first two Gaussian models are 0.53 keV (fixed) and 0.705 keV (fixed), respectively. They represent the oxygen fluorescence $K\alpha$ line and the iron fluorescence $L\alpha$ line. The next seven Gaussian models represent the emission lines of Ne IX (0.91 keV), Ne X (1.02 keV), Fe XXIV (1.11 keV), Ne X (1.21 keV), Mg XII (1.34 keV), Mg XI (1.47 keV), and Si XIII (1.85 keV). The

line-width parameter σ is fixed at 0.001 keV. The last three Gaussian models represent the three iron lines (Fe fluorescence line at 6.4 keV, Fe He-like complex at 6.67 keV, and Fe H-like line at 6.97 keV), and the line center energies are fixed.

Figure 6 shows examples of the averaged spectra and their models. We can see the emission lines, in particular the highly ionized ones denoted by red, were dominant around 1 keV in the bright state, and were weaker and weaker during the fading stage of this outburst. Figure 3 displays the unabsorbed flux of the BB component, that of the sum of seven emission lines of neon, iron, magnesium, and silicon, and that of the PL component plus three iron lines in four energy bands. Here, the

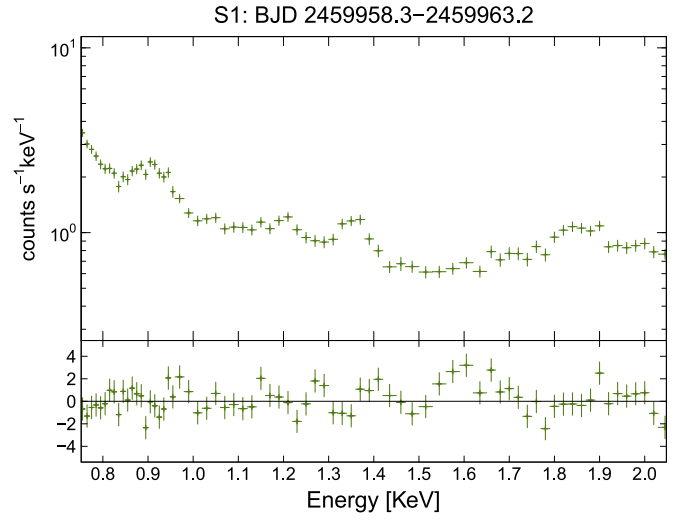


Figure 4. An enlarged figure around 1 keV in a linear energy axis for the spectrum in S1.

"unabsorbed" flux means the flux without interstellar absorption, i.e., $N_{\rm H}$ is zero in the model Tbabs. The intrinsic absorption represented by the model pwab is still multiplied by the PL and three Gaussian components for the multitemperature plasma and iron emission lines in the fourth panel of Figure 3. We also extracted the unabsorbed flux of these components by removing the pwab model (see the fifth panel of the same figure). The BB component was dominant at <1 keV. The total flux of the seven Gaussian models for neon, magnesium, and silicon lines was dominant at 1-2 keV, though its 0.3-1 keV flux became comparable at the end of this outburst. The total flux of the PL plus three Gaussian models was dominant above 2 keV. Although the line flux overwhelmed the flux of the PL component in the 1-2 keV band until the middle of the fading stage, this relation reversed after S6. The PL flux significantly decreased around the outburst maximum. The BB and line fluxes rapidly faded after S6. The PL component was the softest near the outburst maximum.

3.4. Period Analyses

We searched periodic signals from X-ray and optical light curves by using the phase dispersion minimization (PDM) method (R. F. Stellingwerf 1978). Before applying PDM, we subtracted the long-term trend of the light curve by locally weighted polynomial regression (LOWESS; W. S. Cleveland 1979). We determined the length of the data for which the regression should be performed, and the smoother span (f)influencing the smoothness of each data point in this method. In this work, the smoother span ranges between 0.1 and 0.2. We detected a WD spin period of 351.32(8) s from NICER 0.3-8 keV light curves and a 5699(2) s period from AAVSO light curves (see the left and right panels of Figure 7). The 1σ error was computed via the method in J. D. Fernie (1989). Although the latter period was not detected from NICER light curves even during the bright state of this outburst, ~4000-6000 s QPOs were detected from X-ray light curves in previous outbursts (L. Morales-Rueda et al. 1999; S. Vrielmann et al. 2005; P. Zemko et al. 2017). No detection of this period from NICER light curves would be an observational bias since one observational visit by NICER is only \sim 1000 s,

and the time interval between two visits is at least $\sim 1.5 \, \mathrm{hr}$ long.

We applied the same method to NuSTAR 3–10 keV light curves and detected a 351.32(6) s period that is consistent with the WD spin period detected from the NICER light curves (see the middle panel of Figure 7). We did not detect any QPOs from the NuSTAR light curves. Since the NuSTAR data were taken at the end of the outburst, we could not investigate whether QPOs were observable in X-rays during this outburst or not. The continuous observation for the Tomo-e Gozen light curves lasted only for \sim 15 minutes and was too short to search for QPOs. The WD spin signal was not detected at optical wavelengths. Other signals with \sim 320 s and \sim 380 s periods were reported during certain time intervals in previous outbursts of GK Per at optical and X-ray wavelengths (L. Morales-Rueda et al. 1999; D. Nogami et al. 2002). However, we did not detect any signals having these periods.

3.5. Energy Dependence and Time Evolution of White Dwarf Spin Pulses

We divided the NICER data into four time zones: T1, before BJD 2459970; T2, BJD 2459970–2459980; T3, BJD 2459980–2459990; and T4, BJD 2459900–2460000, and made phase-averaged profiles of the WD spin pulse in four energy bands (0.3–1 keV, 1–2 keV, 2–5 keV, and 5–8 keV) in each time zone. These time zones are denoted at the top panel of Figure 2. Here, we fixed the spin period at 351.32 s because we could not detect any variations of this period. We defined the epoch of the light maximum of the phase-averaged profile in the 0.3–8 keV band as T_0 .

Figure 8 shows the resultant pulse profiles. The pulse amplitude at <1 keV was consistently lower than 20%. Although the pulse was dominant at more than 2 keV until T2, the pulse amplitude in the 1-2 keV band became higher after that. The amplitude was highest around the outburst maximum, and the signal rapidly disappeared after T4. The pulse profile was basically single-peaked and not symmetric to phase 0. Double-peaked humps occasionally appeared, e.g., the 0.3-1 keV phase-averaged profile in T3. A flat-bottomed profile was observed in T3 in the 1-2 keV band. The rising slope to the light maximum was less steep than the fading slope to the light minimum. The pulse peak in the 0.3-1 keV and 1–2 keV bands shifted to later phases with respect to those in the 2–5 keV and 5–8 keV bands. The shift of T_0 was 0.2 phases from T1 to T4, which would come from the accuracy of our estimated spin period.

We also investigated the energy dependence of pulse profiles in harder energy bands by using NuSTAR data. Figure 9 shows the result. The epoch is the same as that of T4, as determined by the NICER light curve. The profile is double-peaked, and the amplitude has almost no energy dependence.

We next tried the modeling of on-pulse and off-pulse spectra in T1–T4. Here, "on-pulse" and "off-pulse" spectra indicate spectra for the spin pulse phase -0.1 to 0.1 and the spin pulse phase 0.4 to 0.6, respectively. The applied model is the same as that used in Section 3.3. The spectra and the best-fit models are shown in Figure 10. The PL flux drastically changed between the on-pulse and off-pulse phases, while the the BB and line fluxes did not change very much.

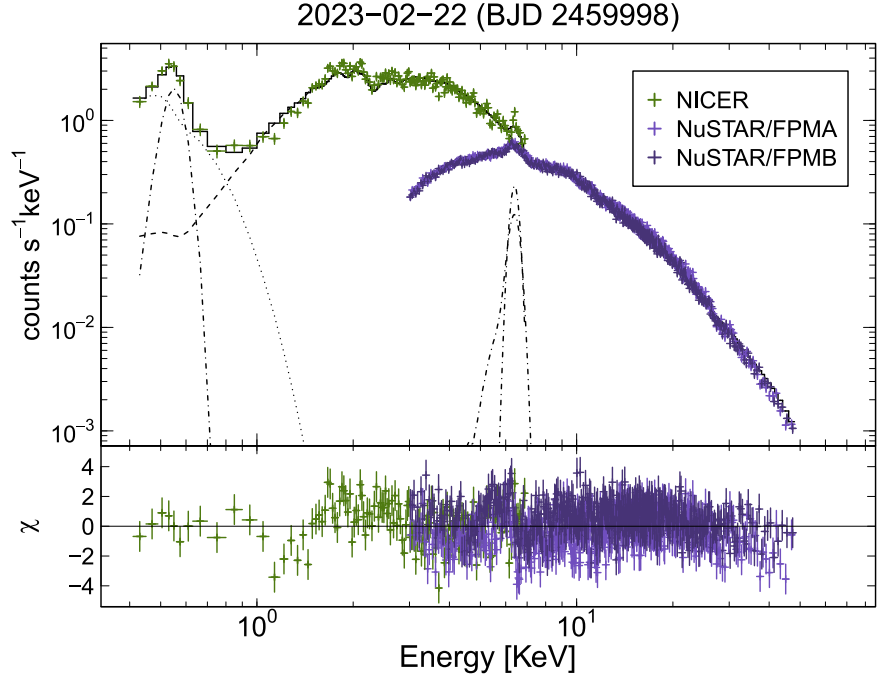


Figure 5. Broadband X-ray spectrum of GK Per on BJD 2459998 (2023 February 22), overlaid with the best-fit spectral model of \texttt{Tbabs}^* ($\texttt{bbody} + \texttt{gaussian} + \texttt{pwab}^*$ ($\texttt{reflect}^*\texttt{vmcflow} + \texttt{gaussian}$). The green crosses represent the NICER data. The purple and dark purple crosses represent the NuSTAR FPMA and FPMB data, respectively. The dot, dashed, and dotted—dashed lines represent the best-fit model components of the BB, cooling flow, and emission lines, respectively. The solid line shows the total best-fit model emission. The normalization of the NuSTAR spectral energy distribution (SED) was 0.98 of the NICER SED.

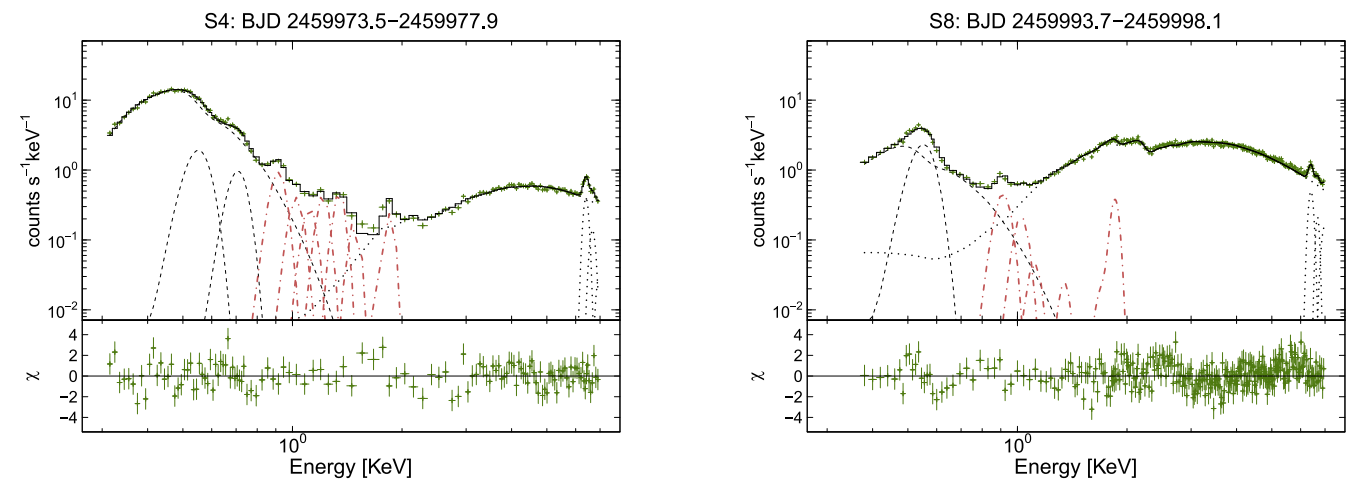


Figure 6. X-ray spectra of GK Per during the 2023 outburst, overlaid with the best-fit spectral model of Tbabs* (gaussian + gaussian + bbody + gaussian +

3.6. Correlation between X-Ray and Optical Fast Variability

High-speed optical photometry of GK Per with Tomo-e Gozen was performed on four nights, and in total two visits were completely overlapped with the NICER observations. The simultaneously observed X-ray and optical light curves are displayed in Figure 11. Here, the optical light curve was binned in 5 s bins, the same as the NICER light curve. The amplitude of optical variations was much smaller than that of

the X-ray ones in these two windows. The variations of the optical light curve of GK Per were larger than that of the neighbor star (USNO A2.0 1275-02381887). However, atmospheric fluctuations could have affected the observed light curve of GK Per, since the light curve of the neighbor star also fluctuated by 0.04 mag within 2σ . Although the gradual increase of the flux over timescales of \sim 0.01 day could be due to intrinsic variations in GK Per, the steep drop of the flux

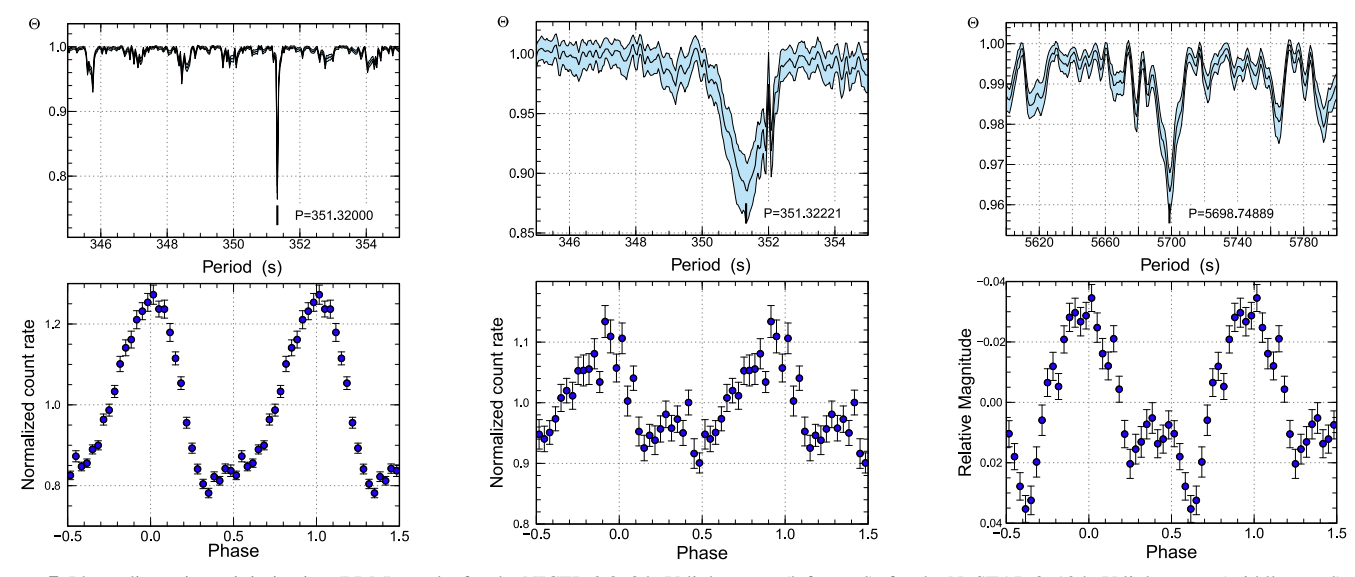


Figure 7. Phase dispersion minimization (PDM) results for the NICER 0.3–8 keV light curve (left panel), for the NuSTAR 3–10 keV light curve (middle panel), and for the optical V-band light curve (right panel) during the 2023 outburst in GK Per. Upper and lower panels represent Θ -diagrams of our PDM analyses and phase-averaged profiles, respectively. The cyan region in the upper panels represents the 90% confidence interval.

around BJD 2459996.966 and the sharp increase of the flux around BJD 2459997.031 would be a kind of atmospheric fluctuation. The intrinsic variations are likely flickering, which has been well-observed in this system (A. Bruch 2021).

We investigated the correlation between the X-ray and optical modulations using cross-correlation function (CCF) analysis. The calculation method for CCF is described in, e.g., J. Patterson & J. C. Raymond (1985) and P. Gandhi et al. (2010). The optical light curves are resampled to a 5 s time bin, which is the same as the X-ray one. Before CCF analyses, we subtracted the long-term light-curve trend from these light curves using LOWESS (W. S. Cleveland 1979), as done in Section 3.4. The smoother span ranged between 0.2 and 1.0. The resultant CCFs are given in Figure 12. The positive lag represents the lag of optical variations to X-ray variations. No significant correlation was detected.

4. Discussion

4.1. Origins of X-Ray Emission Sources

We performed the modeling of X-ray spectra in Sections 3.2 and 3.3. The main emission components are (1) BB emission, which is dominant at <1 keV; (2) several emission lines of neon, magnesium, iron, and silicon, which are dominant in the 1–2 keV range; and (3) multitemperature bremsstrahlung emission, which is dominant at >2 keV. Component (3) is regarded as the emission from the high-temperature and optically thin AC. Component (1) is interpreted as the emission from a part of the WD surface reprocessed and heated by hard X-ray photons from the AC.

The origin of component (2) is under debate (P. Zemko et al. 2017; S. Pei et al. 2024). The absorption was ineffective for source (2) in the off-pulse phase during the 2023 outburst (see Section 3.5), which suggests that the emission source was located outside of the curtain. P. Zemko et al. (2017) showed no excess of nitrogen abundance, which implies that the emission source is unlikely a nova shell irradiated by hard X-rays from the AC. We consider the possible origin as photoionization of the time-varying low-temperature gas of the inner region of the accretion disk and/or the disk wind, since

the line emission became much weaker at the fading stage of this outburst despite little change in the hard X-ray emission from the AC (see Figures 5). For instance, K. Mukai et al. (2003) found that the high-resolution spectrum in GK Per resembled the expectation for photoionized plasma. However, our results cannot settle the issue of whether collisional ionization or photoionization reproduces the spectrum in 1–2 keV (see also the texts in Section 3.3).

4.2. Interpretation of X-Ray Light Curves

On the basis of the interpretation in Section 4.1, we can regard that Figure 3 shows the time evolution of X-ray emission from the three main components of the WD surface, the line emitter, and the AC. We interpret below what the three X-ray light curves in the bottom panel of Figure 2 represent. First of all, we consider the time evolution of the AC flux with increasing mass-accretion rates onto the WD, denoted by $\dot{M}_{\rm acc}$. If $\dot{M}_{\rm acc}$ becomes higher, the column density of the curtain becomes higher, and more X-ray photons from the AC are absorbed. The absorption is effective not only for the 2-5 keV band but also for the 5-8 keV band. The 2-5 keV and 5-8 keV model fluxes of the PL component were lower if the system was brighter at optical wavelengths (see the top and fourth panels of Figure 3). The 2–8 keV light curve in the bottom panel of Figure 2 reflects the AC flux absorbed by the curtain. The flux dropped around the outburst maximum since the column density of the curtain increased with the increase in $\dot{M}_{\rm acc}$.

To interpret the unabsorbed PL flux in the fifth panel of Figure 3, the increase in soft X-ray photons accompanied by the shrinkage in the inner-disk edge should be taken into account. If $\dot{M}_{\rm acc}$ becomes higher, the ram pressure will be higher, and the radius of the inner-disk edge $(r_{\rm in})$ smaller. Then, the shock temperature $(T_{\rm sh})$ of the AC decreases since the freefall velocity of the gas decreases (see, e.g., Equation (5) in Y. Wada et al. 2018). As a result, the X-ray spectrum would become softer. The inferred X-ray luminosity would decrease if the AC becomes optically thick. This phenomenon

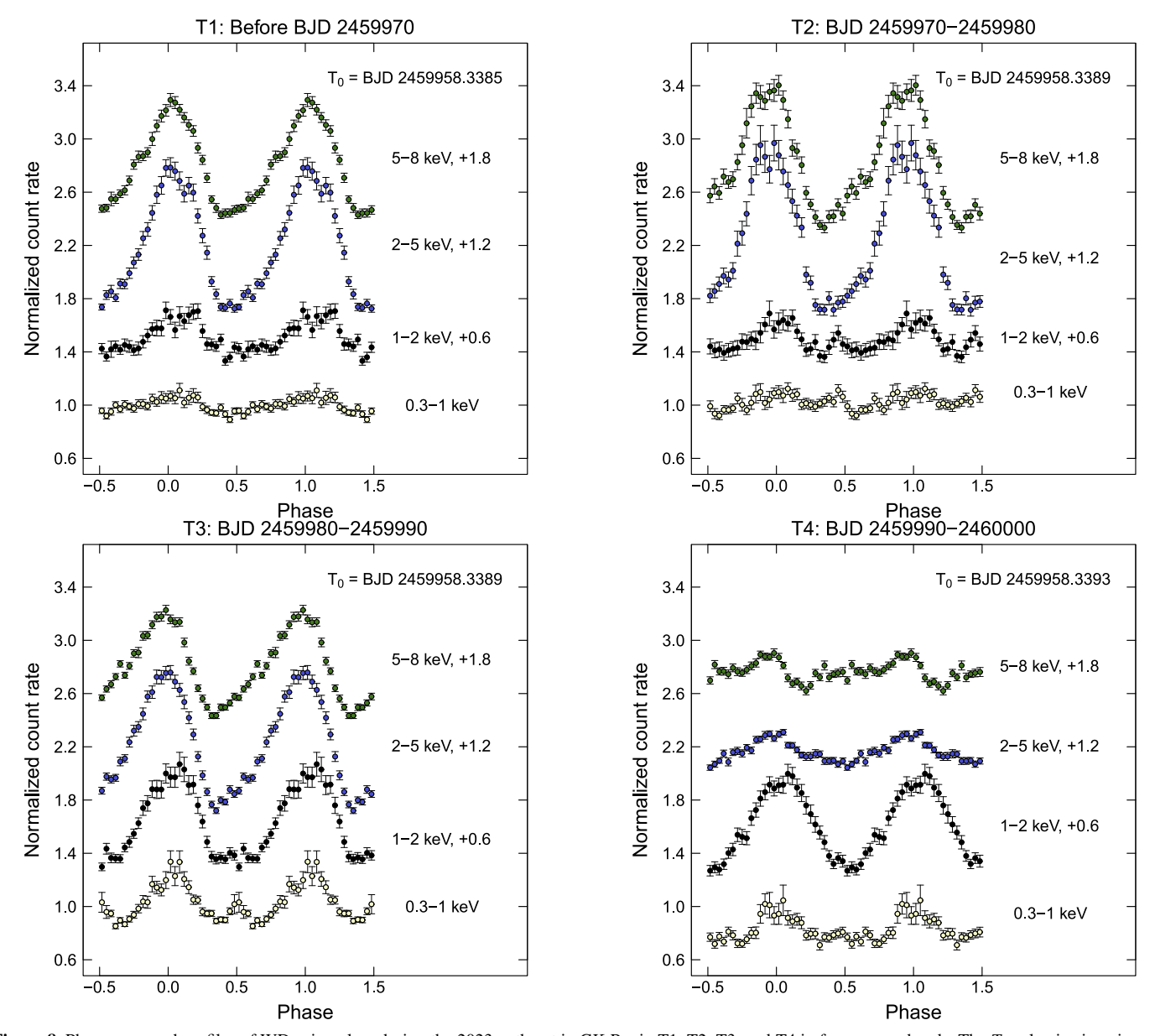


Figure 8. Phase-averaged profiles of WD spin pulses during the 2023 outburst in GK Per in T1, T2, T3, and T4 in four energy bands. The T_0 value is given in each panel. The 1–2 keV, 2–5 keV, and 5–8 keV profiles are shifted vertically for visibility. These offset values are given in each panel.

could explain why the intrinsic X-ray flux from the AC decreased if the system became brighter in optical.

Next, we consider the evolution of the BB flux originating from the irradiated WD surface, as imprinted on the 0.3–1 keV light curve in the bottom panel of Figure 2. The evolution of the BB flux should be related to that of the AC via the irradiation process. The BB flux decreased around the outburst maximum when the unabsorbed flux of the PL component of >1 keV decreased. This would be because hard X-ray photons from the AC decreased. The reason for the smaller decrease in the BB flux than that in the AC flux is probably because a part of the AC became optically thick and increased the BB flux.

The BB flux rapidly decreased at the later part of the fading stage, after S6, though the flux level of the PL component at that time was the same level before the outburst maximum. If $\dot{M}_{\rm acc}$ decreases and $r_{\rm in}$ increases, the reflection effect becomes stronger since the spectrum becomes harder with the increase

in $T_{\rm sh}$. Spectral hardening from the fading stage of an outburst to quiescence was reported in previous works (Y. Wada et al. 2018; S. Pei et al. 2024). Electron scattering becomes more dominant than photoelectric absorption at higher energies, $\gtrsim 10~{\rm keV}$ (see Figure 2 in T. Hayashi et al. 2018) and the irradiation effect becomes lower, which results in a drop of the BB flux.

Finally, we consider the evolution of the line flux. The line flux seems to have traced the absorbed flux of the PL component at $>2 \, \mathrm{keV}$ (see the black and white dots in the third panel and the blue and green dots in the fourth panel of Figure 3). However, the rapid decrease of the line flux after S6 is not straightforward, as discussed above for the BB flux. The time variation of the photoionized gas may naturally explain this phenomenon. The inner-disk edge and the disk wind would become more distant from the AC if $\dot{M}_{\rm acc}$ decreased and $r_{\rm in}$ increased. In this case, photoionization becomes weaker even if

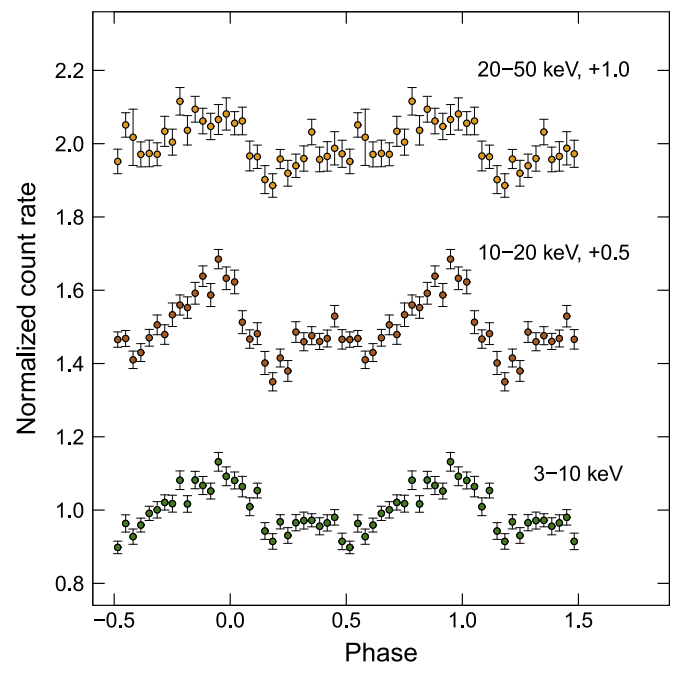


Figure 9. Phase-averaged profiles of WD spin pulses at the end of the 2023 outburst in GK Per in three energy bands. The 10–20 keV and 20–50 keV profiles are shifted vertically for visibility. These offset values are given in this plot.

the X-ray flux from the AC does not change. The $1-2 \,\mathrm{keV}$ light curve in the bottom panel of Figure 2 includes both the emission from the AC and that from the line emitter. The emission from the AC became dominant after the middle of the fading stage (see the bottom panel of Figure 3). The flux slightly increased at the end of this outburst because the column density of the curtain became lower with the decrease in $\dot{M}_{\rm acc}$.

4.3. Can the Volution of White Dwarf Spin Pulses Be Explained by the Accretion-curtain Model?

As shown by the modeling of X-ray spectra, the BB and line fluxes did not change very much between the on-pulse and off-pulse phases (see Figure 10). The main source of the WD spin pulse is the change in the AC flux to the line of sight. The column density of the absorber was much higher in the off-pulse phase than in the on-pulse phase, which suggests that the absorption of the AC created the pulse signal during the 2023 outburst in GK Per.

Since the AC emission was dominant at >2 keV in T1 and T2, the amplitude of spin pulses of <2 keV was low. After the outburst maximum, the AC flux overwhelmed the line flux even in the 1–2 keV band (see the bottom panel of Figure 3), and the pulse amplitude in the 1–2 keV band increased in T3 (see Figure 8). The brighter the system was at optical wavelengths, the higher the pulse amplitude of >2 keV was, which is consistent with more X-ray photons being absorbed with increasing $\dot{M}_{\rm acc}$. The growing pulse amplitude with increasing mass-accretion rate during the 2018 outburst in this system was reported by S. Pei et al. (2024). The amplitude was higher in the 2–5 keV band than in the 5–8 keV band (see Figure 8). This energy dependence was weaker when the system was brighter (see also Figure 10), which can be explained by the change in the column density of the curtain.

If we were to observe both of the magnetic poles of the WD, the pulse profile should be double-peaked. However, the pulse profile is basically single-peaked (see Figure 8). This would be because the magnetic pole below the disk equatorial plane is hidden by the extended inner part of the disk. This idea was proposed by C. Hellier et al. (2004). The profile at the end of the 2023 outburst became double-peaked (see Figure 9), which would indicate the expansion of the inner-disk edge due to the decrease in $\dot{M}_{\rm acc}$. On the other hand, a small hump around phase 0.5 was observed in T3 in the 0.3–1 keV energy band. The irradiated WD surface was wider than the AC, and below the disk equatorial plane it might be observable. Although the BB emission was not sensitive to absorption by the curtain, the change in the surface area visible to the observer can change between the on-pulse and off-pulse phases.

The pulse profile was not symmetric to the peak phase, and the peak phase in the lower-energy bands shifted toward later phases to that in the higher-energy bands (see Figure 8). These observational features could be explained by the twisted geometry of the AC and curtain (see the schematic in Figure 13). If the inner-disk edge is inside of the corotation radius during outbursts, the edge rotates faster than the WD. The magnetic field line from the WD surface is tethered to the disk inner edge, and the disk gas accretes onto the WD along the field line. The field line is dragged toward the direction of rotation. The WD surface irradiated by the AC also would be asymmetric to the center of the AC base.

The above-discussed observational features basically can be explained by the absorption by the curtain. However, we need additional factors to interpret the almost no energy dependence of the high-energy pulse profile at the end of the outburst (see Figure 9). One possible source of this weak energy dependence is electron scattering. According to Figure 2 in T. Hayashi et al. (2018), the mass attenuation coefficient of the incoherent scattering overwhelms that of the photoelectric absorption around 10 keV. If the scattering is effective, we would see a high-energy pulse. Another possible source is the change in the visible area of the AC to the observer between the on-pulse and off-pulse phases, which was pointed out by P. Zemko et al. (2017) as the geometrical effect. If $\dot{M}_{\rm acc}$ decreases, the ram pressure decreases, and the scale height of the AC increases (T. Hayashi & M. Ishida 2014). The visible area of the AC to the observed is maximized at the on-pulse phase. Since the column density of the curtain was low at the end of the outburst, this kind of geometrical effect might generate the pulse signal.

4.4. Possible Origins of Optical Quasi-periodic Oscillations

We detected \sim 5700 s QPOs from the optical light curve (see Section 3.4). B. Warner & P. A. Woudt (2002) proposed that QPO signals are triggered by disk oscillations, which make a vertically thick structure at a part of the disk. The bump on the disk surface is irradiated by high-energy photons from the WD and the inner part of the disk, and the visible area of the irradiated surface of the bumpy structure changes with the Keplerian period at the radius of that structure. For instance, if the gas transferred from the secondary star overflows the outer-disk edge, the overflowing gas impacts around $r_{\rm min}$, given by $r_{\rm min} = 0.0488q^{-0.464}a$, where a is the binary separation (B. Warner 1995; S. Kunze et al. 2001). This process can generate a vertically thick structure at a part of azimuthal angle around $r_{\rm min}$ (S. H. Lubow 1989). In GK Per, $r_{\rm min}$ is 3.9×10^{10} cm. The radius at which the Keplerian period is \sim 5700 s is \sim 5 \times 1010 cm and close to $r_{\rm min}$. The optical QPO

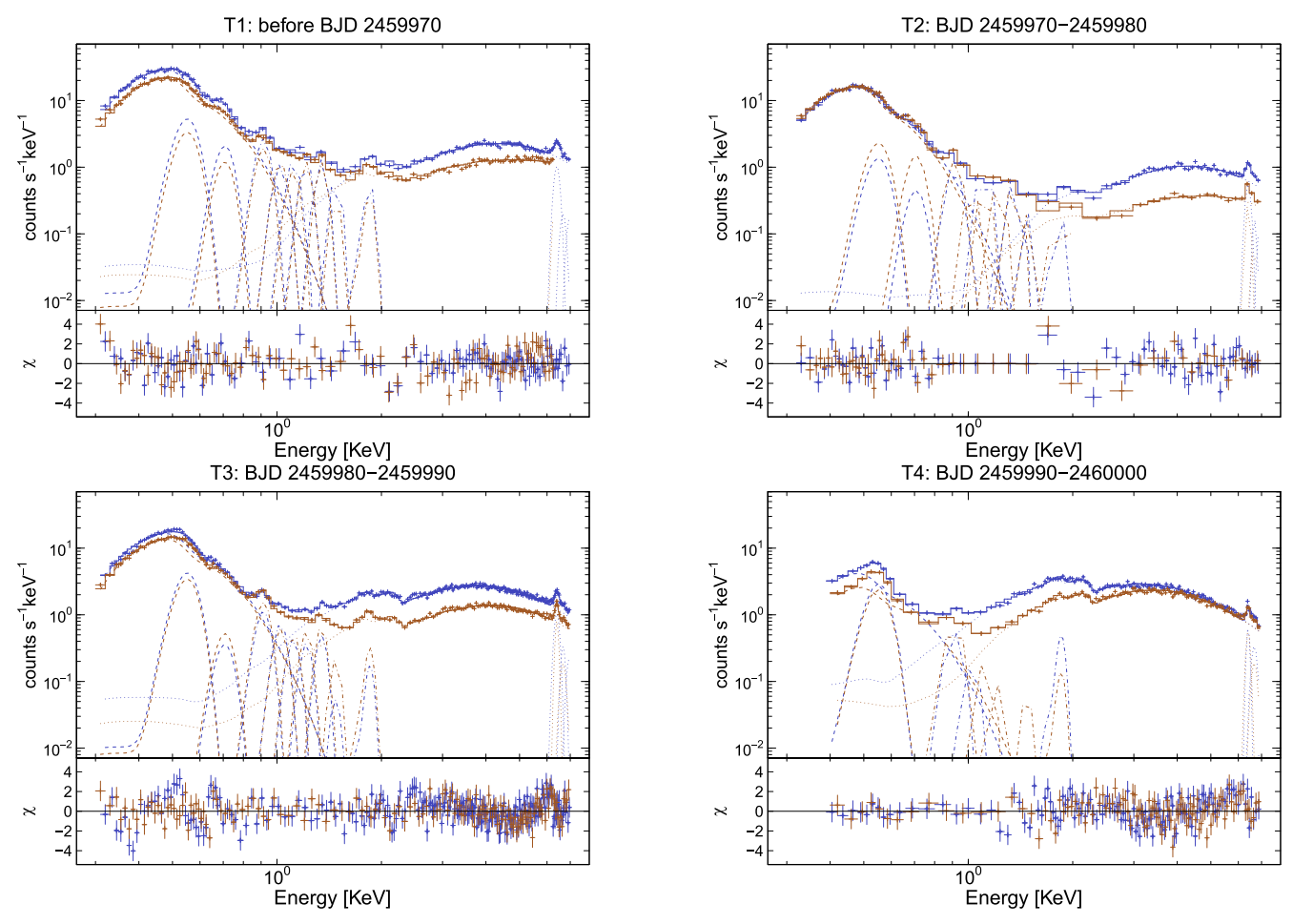


Figure 10. X-ray spectra during the on-pulse and off-pulse phases of GK Per during the 2023 outburst, overlaid with the best-fit spectral model of Tbabs*(gaussian + gaussian + bbody + gaussian + gausian + gaussian + gaussian + gaussian + gaussian + gaussian + gaus

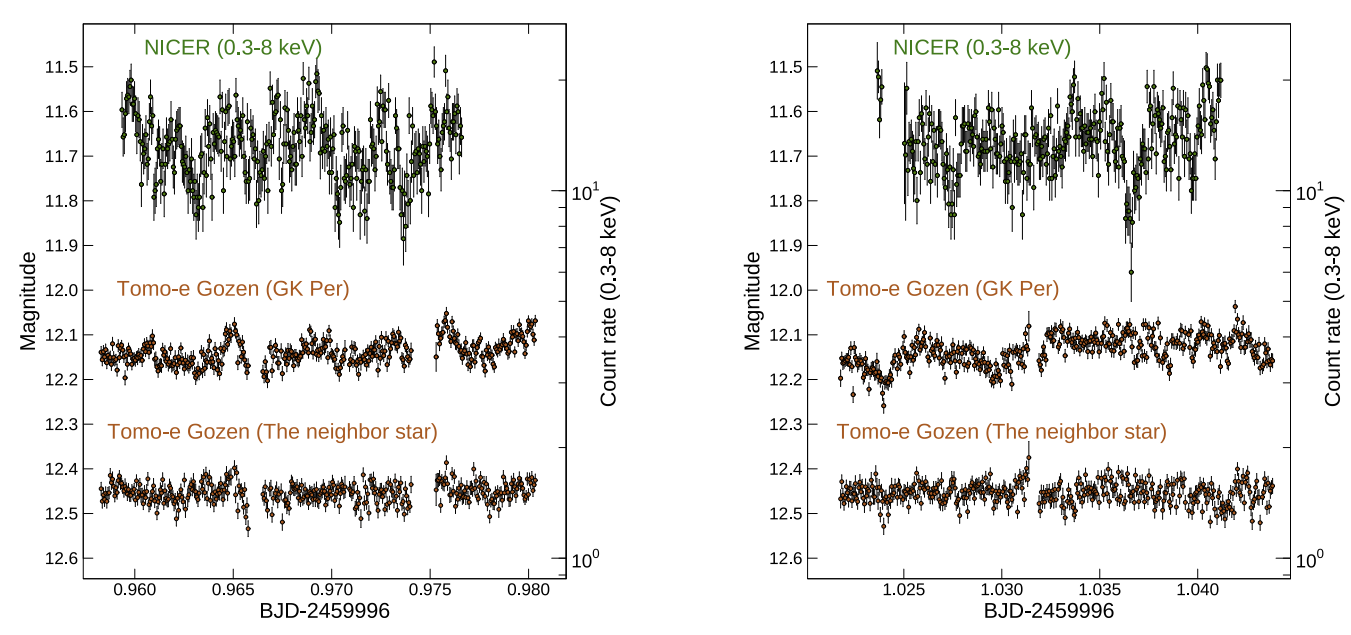
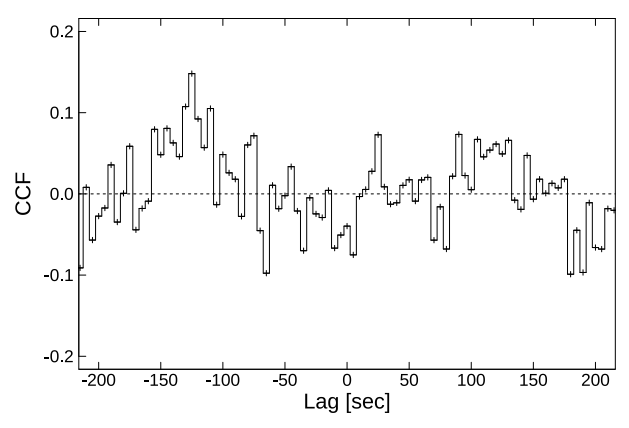


Figure 11. Simultaneously observed X-ray and optical light curves taken by NICER and Tomo-e Gozen on 2023 February 21. The green and orange dots represent the NICER and Tomo-e Gozen light curves, respectively. We also plot the Tomo-e Gozen light curve of the neighbor star USNO A2.0 1275-02381887.



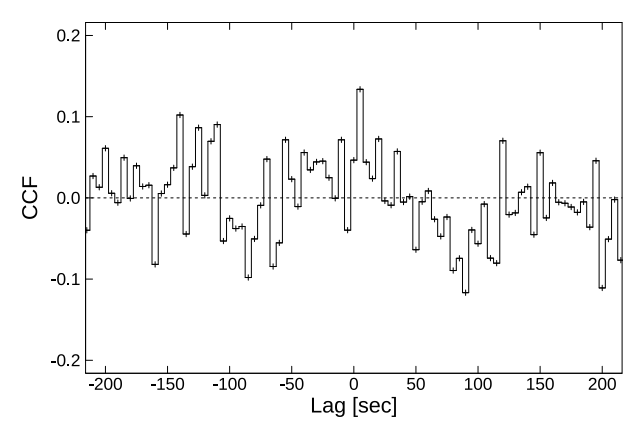


Figure 12. CCFs between the NICER and Tomo-e Gozen light curves of GK Per on 2023 February 21. The positive lag indicates the delay of optical variations to X-ray ones. The data in the left and right panels correspond to the light variations in the left and right panels of Figure 11.

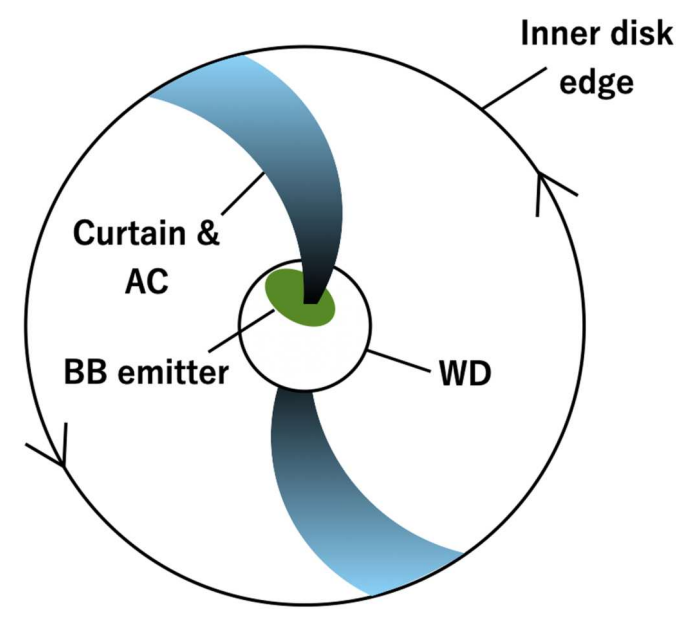


Figure 13. Schematic of the face-on view of the twisted geometry of the AC and the curtain during the 2023 outburst in GK Per. The inner-disk edge rotates counterclockwise. The irradiated WD surface is asymmetric to the center of the AC.

might be caused by the irradiation at the vertically thick structure around this radius. In this case, the QPO period would not change throughout the outburst. We were not able to detect the time evolution of optical QPO periods due to our limited data. More frequent observations are necessary in the future.

Here, we note that the irradiation by X-ray photons from the AC could not reproduce optical QPOs. X-ray photons harder than $\sim\!1$ keV can irradiate the disk gas (L. H. Aller 1959; R. Cruddace et al. 1974). The X-ray luminosity in the 1–50 keV band was $\sim\!4\times10^{34}\,\mathrm{erg\,s^{-1}}$, even at the brightest stage. This was more than 2 orders of magnitudes lower than the intrinsic luminosity of the disk during the outburst in GK Per. In fact, we did not find any strong correlations between the optical and X-ray rapid variations at the end of the outburst (see Section 3.6). The main source of the irradiation would be ultraviolet photons from the WD surface and the inner part of the disk.

4.5. Mechanism of Outbursts in GK Per

Although the outburst in GK Per has some peculiar characteristics, it can be explained by the disk-instability model. The B-V color did not become redder at the onset of the 2023 outburst, which implies that the accretion disk did not drastically expand at the onset of the outburst. The slow-rise optical light curve and slowly hardening PL component are prominent characteristics of inside-out outbursts, and suggest that the heating wave slowly propagated over the disk and that the temperature and the accretion rate of the disk slowly increased (see also Figures 1 and 6). As discussed in M. Kimura et al. (2018), inside-out outbursts tend to be triggered in long-period systems with low mass-transfer rates like GK Per.

Although the simple inside-out outburst shows a linear and slow brightness increase, the rising part of the 2023 outburst in GK Per seems to be complex, and at least two phases would exist. This is interpreted as a representation of the stagnation phase. The thermal equilibrium curve at the outer disk is ξ -shaped rather than S-shaped (S. Mineshige & Y. Osaki 1983; J. K. Cannizzo 1993b). In this case, the outer disk does not always directly jump to the hot state, and temporarily stays at a nonthermal equilibrium intermediate-temperature state during the rise to outburst maximum, as demonstrated by S.-W. Kim et al. (1992) via numerical simulations.

5. Summary

We observed the 2023 outburst of GK Per with NICER, NuSTAR, and Tomo-e Gozen. Our major findings and their interpretations are as follows:

- 1. The optical light curve was consistent with those in past outbursts of this object. We found a steeper rise followed by a slower rise to the outburst maximum. This would be because the outer disk did not directly jump to the hot state. The B-V color evolution implies that the outburst was triggered at the inner part of the disk (see Sections 3.1 and 4.5).
- 2. The broadband X-ray spectrum at the end of the outburst was mainly composed of two emission sources. One is a BB component with a temperature of $\sim 83 \, \text{eV}$, and the other is a multitemperature and optically thin plasma with a maximum temperature of $\sim 54 \, \text{keV}$. The former and the latter represent the emission from the WD

- surface and the AC, respectively (see Sections 3.2 and 4.1).
- 3. The emission from the neon, magnesium, iron, and silicon lines was nonnegligible before the later part of the fading stage during the outburst. These lines were not absorbed in the off-pulse phase, which suggests that they originate from gas outside of the curtain.
- 4. The WD spin pulse, with a 351.3 s period, was observed only in X-rays. The absorption of the AC was much larger in the off-pulse phase than that in the on-pulse phase. These observational features suggest that the spin pulse was reproduced by the absorption of X-ray photons from the AC, which is consistent with the AC model (see Sections 3.4, 3.5, and 4.3).
- 5. The evolution of the pulse amplitude at >2 keV was consistent with a change in the absorption effect by the curtain that occurred with the increase/decrease in the accretion rate onto the WD. The asymmetric pulse profile and the shift of the light maximum of the lower-energy pulse to later phases may be caused by the distorted structure of the AC and curtain due to the inner-disk edge rotating faster than the WD during outburst (see Sections 3.5 and 4.3).
- 6. To explain the almost no energy dependence of highenergy spin pulses at the end of the outburst, we need to introduce a change in the electron scattering effective at >10 keV and/or a change in the visible area of the AC to the observer between the on-pulse and off-pulse phases (see Sections 3.5 and 4.3).
- 7. QPO signals with a 5699 s period were detected from optical light curves. Some kinds of vertically thick structures on the disk surface might be associated with this signal. We may observe periodic changes in the irradiated surface area rotating with the Kepler period (see Sections 3.4 and 4.4).

Our work addressed the mechanism of these unique outbursts, the nature of the X-ray emission, and the origin of the WD spin pulse and its time evolution and energy dependence, as well as the source of the optical QPOs in GK Per. However, there remain unsolved problems. In particular, the source of the neon, magnesium, iron, and silicon emission lines and the origin of the QPOs are unclear. To gain some insight to their nature, we need to perform photoionization simulations and obtain long-term and high-time-cadence light curves during outbursts in the future. Also, obtaining high-resolution spectra and detailed spectral analyses are essential.

Acknowledgments

We are thankful to many amateur observers for providing a lot of data used in this research. This research was partially supported by the Optical and Infrared Synergetic Telescopes for Education and Research (OISTER) program, funded by the Ministry of Education, Culture, Sports, Science and Technology (MEXT) of Japan. This work was financially supported by the Japan Society for the Promotion of Science Grants-in-Aid for Scientific Research (KAKENHI) grant Nos. JP20K22374 (M.K.), JP21K13970 (M.K.), JP21H04491 (S.S., M.K.), and JP24K00673 (W.I.).

ORCID iDs

Mariko Kimura https://orcid.org/0009-0002-1729-8416
Takayuki Hayashi https://orcid.org/0000-0001-6665-2499
Wataru Iwakiri https://orcid.org/0000-0002-0207-9010
Martina Veresvarska https://orcid.org/0000-0002-0146-3096
Simone Scaringi https://orcid.org/0000-0001-5387-7189
Noel Castro-Segura https://orcid.org/0000-0002-5870-0443
Christian Knigge https://orcid.org/0000-0002-1116-2553
Keith C. Gendreau https://orcid.org/0000-0001-7115-2819
Zaven Arzoumanian https://orcid.org/0009-0008-6187-8753

```
References
Aller, L. H. 1959, PASP, 71, 324
Álvarez-Hernández, A., Torres, M. A. P., Rodríguez-Gil, P., et al. 2021,
   MNRAS, 507, 5805
Arnaud, K. A. 1996, in ASP Conf. Ser. 101, Astronomical Data Analysis
   Software and Systems V, ed. G. H. Jacoby & J. Barnes (San Francisco,
Blackburn, J. K., Shaw, R. A., Payne, H. E., Hayes, J. J. E., & Heasarc, 1999
  FTOOLS: A General Package of Software to Manipulate FITS Files,
  Astrophysics Source Code Library, ascl:9912.002
Bradley, L., Sipőcz, B., Robitaille, T., et al. 2024, astropy/photutils: v2.0.2,
  Zenodo: 10.5281/zenodo.13989456
Bruch, A. 2021, MNRAS, 503, 953
Cannizzo, J. K. 1993a, in Accretion Disks in Compact Stellar Systems, ed.
  J. C. Wheeler (Singapore: World Scientific), 6
Cannizzo, J. K. 1993b, ApJ, 419, 318
Cleveland, W. S. 1979, JASA, 74, 829
Cruddace, R., Paresce, F., Bowyer, S., & Lampton, M. 1974, ApJ, 187,
Dobrotka, A., Ness, J. U., Mineshige, S., & Nucita, A. A. 2017, MNRAS,
  468, 1183
Evans, P. A., & Hellier, C. 2007, ApJ, 663, 1277
Fernie, J. D. 1989, PASP, 101, 225
Gaia Collaboration, Brown, A. G. A., Vallenari, A., et al. 2021, A&A, 649,
Gaia Collaboration, Vallenari, A., Brown, A. G. A., et al. 2023, A&A, 674, A1
Gandhi, P., Dhillon, V. S., Durant, M., et al. 2010, MNRAS, 407, 2166
Gendreau, K. C., Arzoumanian, Z., Adkins, P. W., et al. 2016, Proc. SPIE,
  9905, 99051H
Godon, P., Shara, M. M., Sion, E. M., & Zurek, D. 2017, ApJ, 850, 146
Hale, G. E. 1901, ApJ, 13, 173
Hameury, J.-M. 2002, in ASP Conf. Ser. 261, The Physics of Cataclysmic
   Variables and Related Objects, ed. B. T. Gänsicke, K. Beuermann, &
  K. Reinsch (San Francisco, CA: ASP), 377
Hameury, J. M., & Lasota, J. P. 2017, A&A, 602, A102
Harrison, F. A., Craig, W. W., Christensen, F. E., et al. 2013, ApJ, 770, 103
Hayashi, T., & Ishida, M. 2014, MNRAS, 441, 3718
Hayashi, T., Ishida, M., Terada, Y., Bamba, A., & Shionome, T. 2011, PASJ,
  63. S739
Hayashi, T., Kitaguchi, T., & Ishida, M. 2018, MNRAS, 474, 1810
Hellier, C., Cropper, M., & Mason, K. O. 1991, MNRAS, 248, 233
Hellier, C., Harmer, S., & Beardmore, A. P. 2004, MNRAS, 349, 710
Hellier, C., Mukai, K., & Beardmore, A. P. 1997, MNRAS, 292, 397
Henden, A. A., Templeton, M., Terrell, D., et al. 2016, yCat, 2336, 0
Ishioka, R., Uemura, M., Matsumoto, K., et al. 2002, A&A, 381, L41
Kim, S.-W., Wheeler, J. C., & Mineshige, S. 1992, ApJ, 384, 269
Kimura, M., Kato, T., Maehara, H., et al. 2018, PASJ, 70, 78
King, A. R., Ricketts, M. J., & Warwick, R. S. 1979, MNRAS, 187, 77
Knigge, C., Baraffe, I., & Patterson, J. 2011, ApJS, 194, 28
Kunze, S., Speith, R., & Hessman, F. V. 2001, MNRAS, 322, 499
Landi, R., Bassani, L., Dean, A. J., et al. 2009, MNRAS, 392, 630
Lubow, S. H. 1989, ApJ, 340, 1064
Meyer, F., & Meyer-Hofmeister, E. 1981, A&A, 104, L10
Mineshige, S., & Osaki, Y. 1983, PASJ, 35, 377
Mineshige, S., & Osaki, Y. 1985, PASJ, 37, 1
Morales-Rueda, L., Still, M. D., & Roche, P. 1999, MNRAS, 306, 753
Mukai, K., Kinkhabwala, A., Peterson, J. R., Kahn, S. M., & Paerels, F. 2003,
  ApJL, 586, L77
Mukai, K., Rana, V., Bernardini, F., & de Martino, D. 2015, ApJL, 807,
  L30
```

```
Nauenberg, M. 1972, ApJ, 175, 417

Nogami, D., Kato, T., & Baba, H. 2002, PASJ, 54, 987

Osaki, Y. 1996, PASP, 108, 39

Patterson, J., & Raymond, J. C. 1985, ApJ, 292, 535

Pei, S., Orio, M., & Zhang, X. 2024, MNRAS, 529, 1463

Pickering, E. C. 1901, ApJ, 13, 170

Ritter, H., & Kolb, U. 2003, A&A, 404, 301

Rosen, S. R., Mason, K. O., & Cordova, F. A. 1988, MNRAS, 231, 549

Sako, S., Ohsawa, R., Takahashi, H., et al. 2018, Proc. SPIE, 10702, 107020J

Smak, J. 1984, PASP, 96, 5

Stellingwerf, R. F. 1978, ApJ, 224, 953

Suleimanov, V., Doroshenko, V., Ducci, L., Zhukov, G. V., & Werner, K. 2016, A&A, 591, A35
```

```
Tampo, Y., Nogami, D., Kato, T., et al. 2022, PASJ, 74, 460
Tsujimoto, M., Morihana, K., Hayashi, T., & Kitaguchi, T. 2018, PASJ, 70, 109
Vrielmann, S., Ness, J. U., & Schmitt, J. H. M. M. 2005, A&A, 439, 287
Wada, Y., Yuasa, T., Nakazawa, K., et al. 2018, MNRAS, 474, 1564
Warner, B. 1995, Cataclysmic Variable Stars, Vol. 28 (Cambridge: Cambridge Univ. Press),
Warner, B., & Woudt, P. A. 2002, in ASP Conf. Ser. 261, The Physics of Cataclysmic Variables and Related Objects, ed. B. T. Gänsicke, K. Beuermann, & K. Reinsch (San Francisco, CA: ASP), 406
Watson, M. G., King, A. R., & Osborne, J. 1985, MNRAS, 212, 917
Yuasa, T., Hayashi, T., & Ishida, M. 2016, MNRAS, 459, 779
Zemko, P., Orio, M., Luna, G. J. M., et al. 2017, MNRAS, 469, 476
```